Fast sparse recovery and coherence factor weighting in optoacoustic tomography

Hailong He[a,b,†], Jaya Prakash[a,b,†], Andreas Buehler[a,b], and Vasilis Ntziachristos*[a,b]

[a]Institute for Biological and Medical Imaging, Helmholtz Zentrum München, Ingoldstädter Landstraße 1, 85764 Neuherberg, Germany

[b]Chair for Biological Imaging, Technische Universität München, Ismaninger Str. 22, 81675 München, Germany

ABSTRACT

Sparse recovery algorithms have shown great potential to reconstruct images with limited view datasets in optoacoustic tomography, with a disadvantage of being computational expensive. In this paper, we improve the fast convergent Split Augmented Lagrangian Shrinkage Algorithm (SALSA) method based on least square QR (LSQR) formulation for performing accelerated reconstructions. Further, coherence factor is calculated to weight the final reconstruction result, which can further reduce artifacts arising in limited-view scenarios and acoustically heterogeneous mediums. Several phantom and biological experiments indicate that the accelerated SALSA method with coherence factor (ASALSA-CF) can provide improved reconstructions and much faster convergence compared to existing sparse recovery methods.

Keywords: optoacoustic tomography, model-based reconstruction, sparse recovery method, image quality enhancement

1. INTRODUCTION

Optoacoustic (photoacoustic) imaging combines the advantages of two imaging modalities, i.e. the rich contrast of optical imaging and the high resolution of ultrasonic imaging [1-3]. Optoacoustic imaging technique enables multiscale visualization of absorption chromophores having high spatial resolution in the range of micrometer to millimeter at different imaging depths. The unique capabilities of optoacoustic imaging are in providing anatomical, physiological and molecular information for different biological and preclinical applications [1, 2, 4].

Biological samples are typically irradiated with nanosecond laser pulses. Absorption of the light energy generates broadband ultrasonic waves via thermoelastic expansion; these waves have frequencies ranging from hundreds of kilohertz to many tens of megahertz [3, 5]. The recorded optoacoustic signals are used to reconstruct an image using analytical or model-based algorithms [6, 7]. Analytical inversion scheme, such as spherical radon transform, is widely used due to its simple implementation and high efficiency. In contrary, model-based approaches are capable of incorporating information regarding detection geometry, acoustic attenuation, and transducer properties in the reconstruction process [8], which results in more accurate reconstructions. However, large numbers of repeated sparse matrix-vectors multiplications are needed in the iterative inversion scheme of model-based process, which results in significant computational cost [9, 10].

Accelerated model-based methods were developed to reduce the computation cost [10-12]. For example, the angular discretization method was used to generate the model matrix, which effectively reduced the computational cost and saved memory [10, 11]. Besides, the spatial-temporal information along with low-rank constraint was used in the mode-based process for performing faster computation [15]. Other approaches tried to simplify the calculation of the model-matrix and then perform inversion on parallelization platforms like graphics processing unit (GPU), which enabled real-time model-based reconstruction [12].

A particular challenge in optoacoustic tomography is limited-view datasets. In many applications, the object of interest has limited accessibility due to physical constraints and only a limited-view dataset can be acquired. For example, when imaging a mouse brain in vivo it is typically only possible to acquire photoacoustic signals from one side because the mouse head cannot be completely immersed in water. Such limited-view scenarios impose significant inversion challenges, artifacts may arise and compromise reconstruction accuracy [9].

Photons Plus Ultrasound: Imaging and Sensing 2017, edited by Alexander A. Oraevsky, Lihong V. Wang, Proc. of SPIE Vol. 10064, 100642N · © 2017 SPIE · CCC code: 1605-7422/17/$18 · doi: 10.1117/12.2252501

Sparsity based algorithms were shown to perform significantly more accurate reconstructions on limited view datasets [9]. However, a fundamental problem with sparsity based schemes is the high computational cost, as a huge sparse matrix is involved in the optimization procedure. Moreover, sparse recovery based methods may amplify noise in limited-data scenarios, as sparsity constraint is not differentiable at origin (as the function becomes discontinuous) [13]. Therefore weak signal (of the order of noise) will get amplified. Hence, it is necessary to improve the sparse recovery methods for enabling faster reconstruction with improved accuracy.

In this work, we propose an improved sparse recovery scheme for optoacoustic tomography reconstruction. In order to accelerate the reconstruction process, the sparse method is implemented by using the SALSA approach based on least square QR (LSQR) formulation. Furthermore, coherence factor weighting method is integrated with the reconstruction procedure for suppressing noise and artifacts. The accelerated SALSA method with coherence factor weighting achieves better reconstructions and takes much less computation resource compared to conventional sparse recovery algorithms.

2. MATERIALS AND METHODS

2.1 Acoustic forward problem

Model-based methods are based on numerically modeling the forward optoacoustic problem and using that model in an optimization algorithm [9, 14]. A model of optoacoustic signal propagation is built on a grid. This model can then be inverted and multiplied with the measured signals to form an optoacoustic image. The integral in Eq. (2.5) is discretized to form a model matrix using an interpolated model matrix method to result in the following matrix equation,

$$Ax = b \tag{1}$$

Where b is the recorded data and x is the reconstruction image. A is obtained by linear interpolation of the heating function over the image grid. Efficient inversion of Eq. (1) requires regularization. We selected conventional Tikhonov regularization with parameter (λ), and assuming an initial pressure rise distribution is smoothly varying. The objective function to be minimized in this case is given as,

$$\Omega = \|Ax - b\|_2^2 + \lambda \|x\|_2^2 \tag{2}$$

whereby $\| \ \|_2^2$ represents the L2 norm. The above objective function can be solved using normal equations [15], i.e.,

$$x_{tikh} = (A^T A + \lambda I)^{-1} A^T b \tag{3}$$

However, Eq. (3) is computationally expensive due to the time-consuming matrix inversion. Alternatively, the LSQR approach can be employed [16], i.e.

$$x_{LSQR} = V_k ((B_k^T B_k + \lambda I_k)^{-1} \beta_0 \beta_k^T e_1 \tag{4}$$

where Bk represents a bi-diagonal matrix, Vk is the right orthogonal matrix resulting from Lanczos bidiagonalization [16, 17] and β_0 is defined as $\|b\|_2^2 . e_1$ is $[1 \cdots]^T$. Eq. (4) can be inverted in a faster fashion compared to Eq. (3) since it involves inverting the diagonal matrix, which is computationally efficient.

2.2 Proposed SALSA acceleration with coherence factor

The proposed method is based on applying a sparsity constraint and accelerating the reconstruction with the help of bidiagonal matrices. The accelerated Split Augmented Lagrangian Shrinkage Algorithm (ASALSA) is proposed herein as an improved version of SALSA minimization implemented using Krylov subspace optimization. In this case, the objective function to be minimized is,

$$\Omega = \left\| Ax - b \right\|_2^2 + \lambda \left\| x \right\|_1 \tag{5}$$

Sparsity optimization schemes are expected to offer better performance over conventional Tikhonov regularization for limited projection data [18, 19]. Eq. (2) assumes a smooth solution and hence results in large number of unknowns and resulting in smoothening of edges. Eq. (5) assumes the number of unknowns to be sparse (by considering only non-zero entries) and is known to perform well in limited data scenarios. Eq. (5) is minimized using SALSA scheme, which has demonstrated the fastest convergence among existing sparsity norm based optimization schemes [20]. In this scheme, we utilize a variable splitting approach, wherein a new variable is introduced in the optimization procedure. The above objective function is now split into two quadratic minimizations with the help of the temporary variable (v) given as,

$$\omega = \left\| Ax - b \right\|_2^2 + \alpha \left\| x - v_k - d \right\|_2^2 \tag{6}$$

$$\omega = \lambda \left\| x \right\|_1 + \frac{\alpha}{2} \left\| x_{k+1} - v - d_k \right\|_2^2 \tag{7}$$

where α represents the regularization parameter (depends on the noise). Eq. (6) is solved using a *maximum a posteriori* (MAP) based algorithm to obtain an estimate for initial pressure rise (*x)*. Eq. (7) is minimized to obtain an estimate for *v,* using a soft thresholding operation (which acts as a derivative for sparsity minimization). The update for the alternated direction method of multiplier (ADMM) parameter is given as $d_{k+1} = d_k - (x_{k+1} - v_{k+1})$. The minimization in Eq. (6) and (7) and the ADMM parameter update is repeated until convergence.

The original SALSA algorithm involved inversion of a large matrix during the optimization procedure [20]. To accelerate inversion, we recast the SALSA algorithm, as indicated in Table I, by using the LSQR solver. Faster computations are achieved by using LSQR iterative inversion schemes for enabling accelerated SALSA (termed as ASALSA) reconstruction using the L1-norm based approach. It can be seen that Eq. (2) applies a smoothness constraint ($\left\| x \right\|_2$); hence noise will be smoothed out during reconstruction. Conversely, since Eq. (5) applies sparsity constraint, it may amplify weak signal and noise [13]. To suppress noise amplification and artifacts arising due to limited view data and sparsity constraint, we introduce herein an additional operation using a coherence factor (CF), defined as the ratio between the energy of the coherent sum of optoacoustic signals to the total incoherent energy, i.e.

$$CF(i) = \frac{\left| (x_{recon})_i \right|^2}{N \sum_{i=0}^{N} \left| (x_{back})_i \right|^2} = \frac{\left| (x_{recon})_i \right|^2}{A^T b^2} \tag{8}$$

where N represent the total number of pixels in the reconstructed domain. x_{recon} is the reconstructed image obtained using ASALSA and x_{back} is the backprojection reconstruction. The numerator in Eq. (8) represents the energy of the coherent sum of the signals, and the denominator is the total energy sum. The CF values can be interpreted as a focusing quality index estimated from the measured optoacoustic data, ranging from 0 to 1. It is maximal when all signals emitted by an optoacoustic absorber at position r' arrive in same phase at the different detector positions r. After being projected, real signals will constructively superimpose on their point of origin. In this way, good focusing properties can be achieved and consequently a sharp reconstruction. Conversely, incoherent signals will not superimpose on their point of origin after summation, but rather smear out, overall resulting into degradation of image quality. Weighting the amplitude of each image pixel with the corresponding CF can therefore suppress contributions from incoherent signals, which enables identification of noise/artifacts in the reconstructed image and consequently thresholding them. Therefore, the CF is further used for weighting the reconstructed image given as,

$$x_{recon} = CF.* x_{recon} \tag{9}$$

2.3 Simulation and phantom measurement

In order to test the performance of the proposed method, a printed paper (USAF resolution target, standard inkjet printer with black ink) embedded in a 1.9 cm diameter diffuse agar cylinder (6% by volume Intralipid in the agar solution) was imaged. The absorbing features of the phantom are shown in Fig. 1(a). The phantom consisted of several groups of line elements of different sizes, which can be used for resolution and image quality characterization at different levels. In order to mimic limited-view scenarios, we assumed a down-sampled dataset, employing 128 positions over 135° coverage angle. Furthermore, a mouse kidney was imaged ex-vivo to examine the performance of the proposed method with biological tissue. The kidney sample was extracted post-mortem (non-perfused) according to institutional regulations regarding animal handling protocols and subsequently embedded in a diffuse agar block (6% by volume intralipid in the agar solution) for ensuring uniform illumination of the sample. The phantom and tissue experiments were conducted using a commercial small animal multispectral optoacoustic tomography (MSOT) scanner (Model: MSOT256-TF, iThera Medical GmbH, Munich, Germany) [21, 22].

The performance of reconstructions based on different reconstruction methods was compared using the experimental measurements collected from phantoms and mouse kidneys. Prior to reconstruction, the OA signals were band-pass filtered with cut-off frequencies between 0.2 and 7 MHz in order to remove low frequency off-sets and high frequency noise. A uniform speed of sound of 1510 m/s was used for all the reconstructions. For all phantom measurements, images were reconstructed with a pixel size of 100 μm (200x100 pixels^2), and in the case of tissue data a pixel size of 100 μm (200x180 pixels^2) was used. The regularization parameter for the L2-norm based scheme was obtained using an L-curve approach while in case of ASALSA algorithm, it was chosen heuristically. The parameters α and λ were set as 100 and 1500 for the ASALSA algorithm. Note that in case of ASALSA algorithm, we have multiple parameters (α and λ) which are sensitive to noise, therefore they can be adjusted based on the image quality of the reconstructed image.

3. RESULTS

The reconstruction results corresponding to the printed-paper USAF-resolution phantom using 256 detector elements over 270° are depicted in Fig. 1. Fig. 1(a) shows the structure of the paper phantom. Fig. 1(b) is the image reconstructed by L2-norm scheme whereas Fig. 1(c) indicates the reconstructed image obtained by ASALSA method. Both reconstructions result in similar initial pressure rise distribution. In contrast, the proposed ASALSA-CF method achieves sharper structure and lesser background artifacts compared to the other results. The artifact reduction is apparent from the zoomed in areas shown in the insets of Fig. 1(b)-(d), the zoomed region is indicated by red rectangle in Fig. 1(a). Even though the image intensity of line features (label 1 marked in (b)) is partially distorted, the line profiles along the red dash line indicated in Fig. 1(b) (shown in Fig. 1(e) and (d)), suggest that line features are better resolved in the image reconstructed by the proposed method.

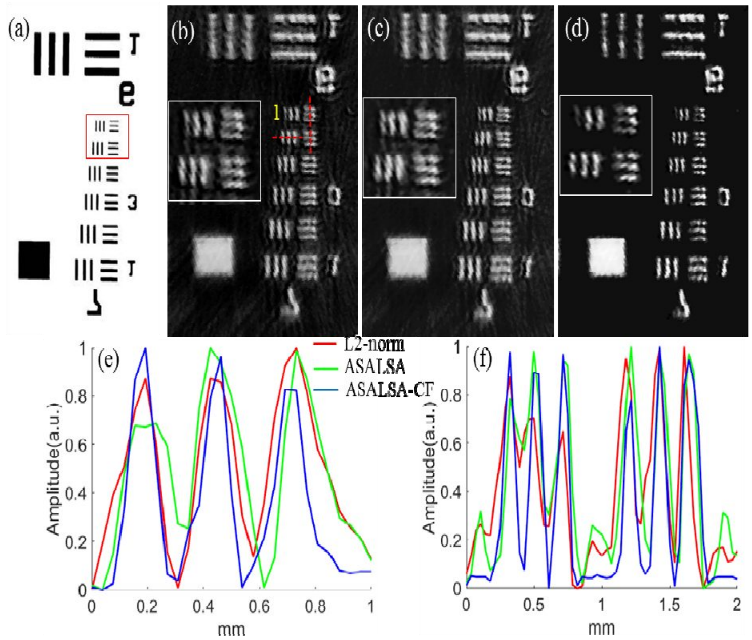

Fig. 1. (a) Reference USAF phantom printed on white paper with black ink, which was embedded in scattering agar. (b) The reconstructed image by L2-norm. (c) ASALSA method and (d) the proposed method. The subsects in (b-d) are the zoom-in of region marked in red rectangle of (a) respectively. The line profiles in the horizontal and vertical directions marked in panel (b) are represented in (e) and (f) respectively.

Underdamped data with limited-view condition (128 transducer positions over 135 degrees) are reconstructed and the corresponding results are shown in Fig. 2. The L2-norm based reconstruction is fully distorted and blurred. Line features (labels 1 and 2) in Fig 2(a) cannot be identified. In contrast, the ASALSA method shows better performance in resolving the line pattern. Clearly, both images contain artifacts and blurry regions. However, Fig. 2(c) shows fewer artifacts and line features are much better distinguishable compared to the other reconstruction results indicating the superiority of the proposed scheme. Line profiles and zoomed images present similar resolution improvement as in previous cases. Meanwhile, the CNR values of line features (yellow labels 1, 2, 3 and 4) are calculated and displayed in Table 1. It can be seen that the ASALSA-CF method achieve better image contrast than the other methods.

TABLE 1
CONTRAST (CNR) COMPARISON

Methods	OBJECT 1	OBJECT 2	OBJECT 3	OBJECT 4
L2-norm	0.1(D[a])	0.4(D)	0.2(D)	1.4
SALSA	0.9	0.7	1.2	2.1
ASALSA-CF	1.2	1.4	2.4	3.7

D[a]: Distorted

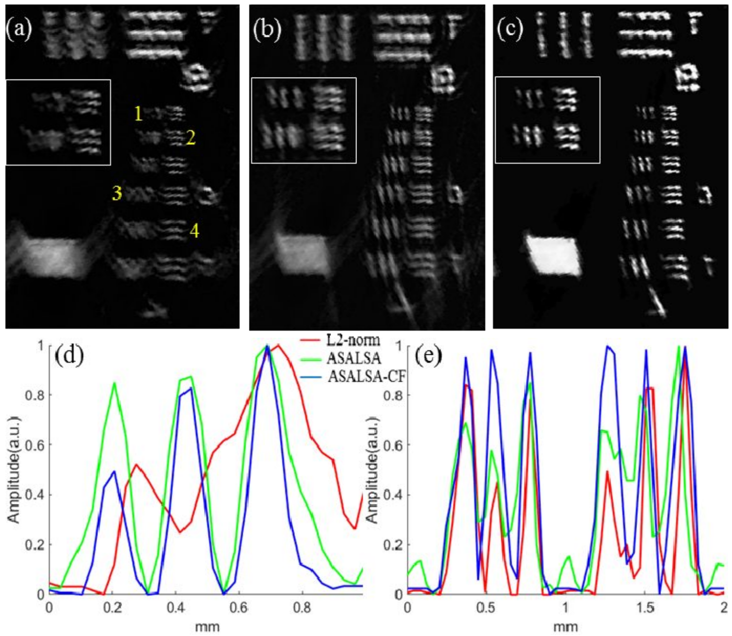

Fig. 2. Images reconstructed using 128 transducer positions over 135 degrees. (a) The reconstructed image by L2-norm. (b) ASALSA and (d) the proposed method. The subsects in (a-c) are the zoom-in of region marked in red rectangle of Fig. 1(a) respectively. The line profiles in the horizontal and vertical directions marked in panel Fig. 1(a) are represented in (d) and (e) respectively.

The results pertaining to the *ex-vivo* kidney experiment reconstructed from 256 elements over 270 degrees are presented in Fig. 3. Fig. 3(a) and (b) shows images obtained with the L2-norm and ASALSA method. In analogy to the paper phantom, these two images display similar image quality. However, the CF method further improves the reconstruction performance of the SALSA scheme, as illustrated in Fig. 3(c) showing improved reconstruction quality. Specifically, blood vessel structures marked with the box indicated on Fig. 3(a) are better distinguishable and less blurry with the ASALSA-CF approach compared to other scheme (insets of Figs. 3(a-c)). The visual evaluation is further corroborated by the line profile drawn over a given image segment [indicated by the dash line in Fig. 3(a)], which indicates that blood vessels marked by the red line are better resolved in the ASALSA-CF reconstructions.

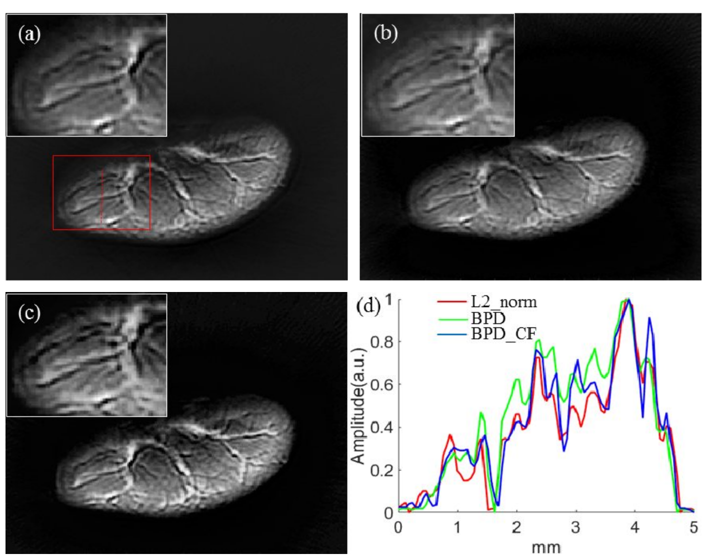

Fig. 3. Reconstructed images of the mouse kidney from 256 transducer positions over 270 degrees. (a) the reconstructed image by L2-norm. (b) ASALSA method and (d) the proposed method. The subsects in (a-c) are the zoom-in of region marked in red rectangle of Fig. 3(a) respectively. The line profiles marked by the red line in panel Fig. 3(a) is represented in (d).

The comparison of different reconstruction schemes with respect to the computational time and memory requirements is presented in Table 2. We calculated the reconstruction time and memory usage for Fig. 1 and Fig. 2 using a normal PC (Intel Core i5-3470 @2.3GHz and 16 GB memory). It can be seen from Table-II that the proposed method takes more time and memory compared to the L2-norm approach. However, the conventional SALSA method cannot reconstruct the 256 signals because of computer memory limitation. For 128 signals, the original SALSA method is over 20 times slower and takes 7 times more memory compared to the proposed method.

TABLE 2
COMPUTATION TIME(S) AND MEMORY (GB)

Methods	FIG.1	FIG.2
L2-norm	79/2.5	35/1.3
SALSA	Out of memory	3554/14.7
ASALSA_CF	294/4.7	137/2.2

4. CONCLUSION

In this work, we proposed a fast sparse recovery method along with coherence factor weighting for optoacoustic tomographic image reconstruction. The interpolated model matrix method employs a sparse matrix; hence it is beneficial to utilize mathematical tools pertaining to sparse algebra. Therefore the original Basis Pursuit (solved using Augmented Lagrangian method) is rewritten using iterative Krylov subspace solvers (LSQR inversion), which tends to converge in fewer iterations. It has been proved that the accelerated SALSA approach can save enormous memory and significantly accelerate the computation time compared to the original SALSA approach.

Funding. Andreas Buehler acknowledges funding from the European Union project FAMOS (FP7 ICT, contract no. 317744). JP acknowledges Alexander von Humboldt Postdoctoral Fellowship program. JP also acknowledges initial discussion with Dr. Calvin B. Shaw.

REFERENCES

[1] A. Taruttis, G. M. van Dam, and V. Ntziachristos, "Mesoscopic and Macroscopic Optoacoustic Imaging of Cancer," Cancer Res, 75(8), 1548-1559 (2015).

[2] A. Taruttis, and V. Ntziachristos, "Advances in real-time multispectral optoacoustic imaging and its applications," Nature Photonics, 9(4), 219-227 (2015).

[3] P. Beard, "Biomedical photoacoustic imaging," Interface Focus, 1(4), 602-31 (2011).

[4] V. Ntziachristos, and D. Razansky, "Molecular imaging by means of multispectral optoacoustic tomography (MSOT)," Chem Rev, 110(5), 2783-94 (2010).

[5] X. L. Dean-Ben, D. Razansky, and V. Ntziachristos, "The effects of acoustic attenuation in optoacoustic signals," Phys Med Biol, 56(18), 6129-48 (2011).

[6] M. Xu, and L. Wang, "Universal back-projection algorithm for photoacoustic computed tomography," Physical Review E, 71(1), (2005).

[7] A. Rosenthal, V. Ntziachristos, and D. Razansky, "Acoustic Inversion in Optoacoustic Tomography: A Review," Curr Med Imaging Rev, 9(4), 318-336 (2013).

[8] A. Rosenthal, V. Ntziachristos, and D. Razansky, "Optoacoustic methods for frequency calibration of ultrasonic sensors," IEEE Trans Ultrason Ferroelectr Freq Control, 58(2), 316-26 (2011).

[9] A. Buehler, A. Rosenthal, T. Jetzfellner *et al.*, "Model-based optoacoustic inversions with incomplete projection data," Medical Physics, 38(3), 1694 (2011).

[10] X. L. Dean-Ben, V. Ntziachristos, and D. Razansky, "Acceleration of optoacoustic model-based reconstruction using angular image discretization," IEEE Trans Med Imaging, 31(5), 1154-62 (2012).

[11] K. Wang, J. Xia, C. Li *et al.*, "Fast spatiotemporal image reconstruction based on low-rank matrix estimation for dynamic photoacoustic computed tomography," J Biomed Opt, 19(5), 056007 (2014).

[12] L. Ding, X. L. Dean-Ben, and D. Razansky, "Real-time Model-based Inversion in Cross-sectional Optoacoustic Tomography," IEEE Trans Med Imaging, (2016).

[13] K. Lee, Y. Bresler, and M. Junge, "Subspace Methods for Joint Sparse Recovery," IEEE Transactions on Information Theory, 58(6), 3613-3641 (2012).

[14] A. Rosenthal, D. Razansky, and V. Ntziachristos, "Quantitative optoacoustic signal extraction using sparse signal representation," IEEE Trans Med Imaging, 28(12), 1997-2006 (2009).

[15] D. Calvetti, S. Morigi, L. Reichel *et al.*, "Tikhonov regularization and the L-curve for large discrete ill-posed problems," Journal of Computational and Applied Mathematics, 123(1-2), 423-446 (2000).

[16] C. C. P. a. M. A. Saunders, "LSQR: An algorithm for sparse linear- equations and sparse least-squares," Journal ACM Transactions on Mathematical Software, 8(1), 43-71 (1982).

[17] J. Prakash, and P. K. Yalavarthy, "A LSQR-type method provides a computationally efficient automated optimal choice of regularization parameter in diffuse optical tomography," Med Phys, 40(3), 033101 (2013).

[18] M. Lustig, D. Donoho, and J. M. Pauly, "Sparse MRI: The application of compressed sensing for rapid MR imaging," Magn Reson Med, 58(6), 1182-95 (2007).

[19] J. Prakash, C. B. Shaw, R. Manjappa *et al.*, "Sparse Recovery Methods Hold Promise for Diffuse Optical Tomographic Image Reconstruction," IEEE Journal of Selected Topics in Quantum Electronics, 20(2), 74-82 (2014).

[20] M. V. Afonso, J. M. Bioucas-Dias, and M. A. T. Figueiredo, "Fast Image Recovery Using Variable Splitting and Constrained Optimization," Ieee Transactions on Image Processing, 19(9), 2345-2356 (2010).

[21] D. Razansky, A. Buehler, and V. Ntziachristos, "Volumetric real-time multispectral optoacoustic tomography of biomarkers," Nat Protoc, 6(8), 1121-9 (2011).

[22] A. Buehler, E. Herzog, D. Razansky *et al.*, "Video rate optoacoustic tomography of mouse kidney perfusion," Opt Lett, 35(14), 2475-7 (2010).